Biogeochemical fluxes of nickel in the global oceans inferred from a diagnostic model

Seth G. John[1], Benoît Pasquier[1,2], Mark Holzer[2], Sam Silva[1]

[1]Department of Earth Sciences, University of Southern California, Los Angeles, CA, USA.
[2]School of Mathematics and Statistics, University of New South Wales, Sydney, NSW, Australia

Corresponding author: Seth John (sethjohn@usc.edu)

Abstract

Nickel (Ni) is a micronutrient that plays a role in nitrogen uptake and fixation in the modern ocean may have impacted rates of methanogenesis on geological timescales. Here we present the results of a diagnostic model of global ocean Ni fluxes which addresses key questions about the biogeochemical processes which cycle Ni in the modern oceans. Our approach starts with extrapolating the sparse available observations of Ni data from the GEOTRACES project into a global gridded climatology of ocean Ni concentrations. Three different machine learning techniques were tested, each relying on marine tracers with better observational coverage such as macronutrient concentrations and physical parameters. The ocean transport of this global Ni concentration field is then estimated using the OCIM2 ocean circulation inverse model, revealing regions of net convergence or divergence. These diagnostics are not based on any assumption about Ni biogeochemical cycling, but their spatial patterns can be interpreted as reflecting biogeochemical processes. We find that the spatial pattern of Ni uptake in the surface ocean is similar to phosphate (P) uptake, but not silicate (Si) uptake, suggesting that Ni is not incorporated into diatom frustules. We find that Ni:P ratios at uptake do not decrease with Ni concentrations approaching 2 nM, which challenges the hypothesis of a ~2 nM pool of non-bioavailable Ni in the surface ocean. Finally, the net regeneration of Ni occurs deeper in the ocean than P remineralization, which could be explained by reversible scavenging or the presence of a refractory Ni phase.

Plain language summary

Nickel is an important micronutrient for algae which live in the oceans. Here we have built a computer model which predicts where algae take nickel out of seawater in the surface ocean, and where they release nickel back into the dissolved phase after they die and sink into the ocean abyss. To build this model we first needed to predict the nickel concentration in global oceans based on a few simple parameters such as temperature, salinity, and the concentration of other nutrients. We then use model output to understand biogeochemical process such as what sorts of phytoplankton take nickel out of seawater, whether hard-shelled diatoms incorporate nickel into their shells (frustules), and whether nickel is adsorbed from the dissolved phase onto sinking particles in the ocean.

1 Introduction

1.1 The cycling of Ni in the global oceans

Nickel (Ni) is a nutrient for phytoplankton in the oceans. It is a cofactor for important enzymes including Ni superoxide dismutase (NiSOD), which detoxifies superoxide radicals (Dupont et al., 2008; Qiu and Price, 2009; Alfano and Cavazza, 2020), urease, which facilitates uptake of the nitrogen from the N-containing molecule urea (Dupont et al., 2008; Biscéré et al., 2018; Alfano and Cavazza, 2020), and NiFe hydrogenase, which catalyzes the reaction of hydrogen gas to protons and electrons and is involved in nitrogen fixation (Tuo et al., 2020). Nickel is also crucial for methanogenesis as a cofactor for the enzyme methyl-coenzyme M reductase (MCR), leading to the speculation that Ni availability in the past oceans played a key role in controlling methanogenesis, and therefore oxygenation of the atmosphere (Konhauser et al., 2009; Wang et al., 2019; Zhao et al., 2021).

Nickel has a nutrient-like distribution in the oceans. It is depleted in the surface ocean compared to the deep ocean, and it exhibits increasing concentrations from the deep Atlantic to the deep Pacific Ocean (Fig. 1), which is characteristic of elements that are incorporated into biological tissue in the surface ocean and regenerated at depth where they accumulate along the deep ocean 'conveyor belt' (John and Sunda, 2018; Schlitzer et al., 2018; GEOTRACES Intermediate Data Product Group, 2021). While these broad patterns in the global distribution of Ni are easily explained, key details of Ni biogeochemical cycling are still debated, including whether Ni is incorporated into diatom frustules and whether all Ni in the surface oceans is bioavailable.

1.2 Key hypotheses regarding the marine biogeochemical cycling of Ni

First we consider the hypothesis that Ni is incorporated into diatom frustules, which arises from experimental and field data on diatoms as well as from patterns in the global distribution of Ni in the oceans. Analysis of diatoms by SXRF mapping shows that large amounts of Ni are present on the outside of diatoms in the same location where Si from diatom frustules is observed (Twining et al., 2012). The addition of silicate (Si) to equatorial waters promoted a large drawdown in Ni, further suggesting that Ni is incorporated into diatom frustules (Twining et al., 2012). This idea is supported by the fact that Ni has a deeper concentration maximum than soft-tissue macronutrients N and P, particularly in the North Pacific, yielding a Ni depth profile which is reminiscent of Si, which is remineralized slower from dissolving diatom frustules and thus deeper in the water column. Incorporation of Ni into the crystal matrix of diatom frustules could explain all of these observations.

However, recent work suggests that Ni is not present in diatom frustules. It was found that nearly all of the Ni in both laboratory-cultured and natural diatoms is found in the HNO_3-soluble soft-tissue, rather than in the HF-soluble silicate frustules (John et al., 2022). A recent biogeochemical model was able to obtain the observed, Si-like, deep regeneration of Ni either through reversible scavenging of Ni onto sinking particulate matter or by slower regeneration of Ni compared to P for some other reason (John et al., 2022).

A second key hypothesis regarding Ni global biogeochemical cycling posits the existence of a refractory Ni pool. That a fraction of dissolved Ni in the surface oceans is not bioavailable has been invoked to explain the fact that Ni is never depleted below ~1.7 nM, compared to maximum deep concentrations around 10 nM, while macronutrients N, P, and Si, and many other trace-metals such as Fe, Zn and Cd are depleted by orders-of-magnitude compared to their deep ocean maxima (John and Sunda, 2018). However, the uptake of Ni in the high-latitudes only depletes Ni down to concentrations around 2 nM in the oligotrophic gyres, leading to the suggestion that

Ni is comprised of biologically-available pool which dominates in the deep ocean, and a separate ~2 nM non-bioavailable pool of Ni which is never depleted in the surface ocean (Price and Morel, 1991; Mackey et al., 2002; Wen et al., 2006). A ~2 nM non-bioavailable pool of Ni has also been invoked to explain patterns of Ni isotopes in the surface oceans, which are anomalously high at lower Ni concentrations compared to what would be expected based on simple Rayleigh fractionation, but could be explained by mixing of bioavailable and non-bioavailable pools of Ni with different δ^{60}Ni signatures (Archer et al., 2020; Lemaitre et al., 2022).

Recent experimental and modeling work calls into question the existence of a non-bioavailable Ni pool. Specifically, it has been shown that Ni in natural seawater is chemically labile to EDTri-A functional groups on Nobias resin, and is biologically available to several species of cyanobacteria and diatoms in culture, when the seawater culture media is amended with extra macronutrients, with both experiments showing that Ni can be drawn down well below the ~2 nM threshold (John et al., 2022). These observations are reconciled with the lack of Ni depletion in oligotrophic gyres by a biogeochemical model in which Ni is depleted slightly more slowly than macronutrients from upwelling waters, such that the ~2 nM Ni observed in oligotrophic gyres is simply the amount of Ni that is 'left over' after macronutrient depletion.

1.3 Prognostic and diagnostic ocean Ni models

The only previous effort to model Ni in the global oceans, of which we are aware, is a mechanistic biogeochemical model, or a 'prognostic' model, built using the AWESOME OCIM framework (John et al., 2020). This model included the processes of biological uptake and remineralization of soft-tissue Ni, and in some cases reversible scavenging of Ni onto sinking particles, all occurring within the realistic global ocean circulation prescribed by OCIM 1.0 (the Ocean Circulation Inverse Model; DeVries, 2014). This prognostic model was able to skillfully reproduce the global distribution of Ni in the global oceans (R^2 = 0.95), and was useful in formulating and evaluating the hypotheses described above.

A different approach for exploring the biogeochemical processes that cycle elements in the ocean is to use what we here call a 'diagnostic' model. Instead of explicitly parameterizing every biogeochemical process, a diagnostic model infers them by other means. Specifically, it is possible to determine if biogeochemical processes add or remove a metal from the dissolved phase from the spatial patterns of other tracers and/or using a model of the ocean circulation. With the advent of global scale trace-metal sampling programs such as GEOTRACES, it has become possible to build such diagnostic models for metals, as has been successfully done for Zn (Roshan et al., 2018), Cu (Roshan et al., 2020), Cd (Roshan and DeVries, 2021), and DOC (Roshan and DeVries, 2017).

The diagnostic modeling approach used here is to calculate the transport of Ni by physical circulation, and infer biogeochemical fluxes of nutrients from any imbalance between transport sources and sinks (Fig. 2). The ocean circulation model completely determines the movement of water between neighboring grid cells. Thus, if the Ni concentration in every model grid cell is known, it becomes possible to calculate the rate at which Ni is being transported into and out of every grid cell.

When performing such calculations for ocean nutrients, it is typical to find a net supply of nutrients into surface ocean grid cells by water transport. This occurs because surface ocean nutrient concentrations are low, while concentrations in nearby subsurface grid cells are higher, so that exchange of water between the surface and subsurface ocean grid cells results in a net upwards flux of dissolved nutrients. Conversely, grid cells deeper in the ocean typically experience a net loss of nutrients by physical transport. As described below, the maintenance of

steady-state nutrient distributions in the ocean thus requires invoking additional processes such as the removal of nutrients from surface waters by phytoplankton uptake, and the addition of nutrients into the deep ocean by remineralization.

Sources and sinks of elements due to physical water transport can be described using various terminology. For example, one might describe a net supply of dissolved nutrients into the surface ocean by water transport as a 'transport flux convergence'. Alternatively, it is common in modeling and engineering to describe flux in terms of their divergences, in which case it would be most accurately described as a 'negative net transport flux divergence'. Colloquially, this could be described as a net supply of nutrients to the surface ocean by transport. In the deep ocean, nutrient elements typically have a positive net transport flux divergence, corresponding to a net loss of nutrients by water transport.

Because of mass conservation, in steady state, the external sources (e.g., remineralization) and sinks (e.g., biological uptake) of a dissolved tracer must balance its flux divergence due to physical circulation only. We emphasize that the key feature of this diagnostic modeling approach is that it does not involve any explicit biogeochemistry calculation. That is, the flux divergence is calculated at every grid cell and highlights the spatial regions over which an element must be added or removed to be in balance, without any assumptions about what sorts of biogeochemical processes would account for this addition or removal. None the less, such calculations of transport divergences often have obvious biogeochemical meanings, for example the negative net transport divergence in the surface ocean reflects uptake of an element by phytoplankton, while the positive net transport divergence in the deep ocean reflects remineralization.

In order to build a diagnostic model such as described above, it is necessary to know the concentration of the dissolved tracer in every model grid cell. This is typically straightforward for macronutrients and other factors for which global climatologies are available (e.g., the World Ocean Atlas). However, even with the dramatic increase in the availability of trace-metal concentration data from the GEOTRACES program (Schlitzer et al., 2018; GEOTRACES Intermediate Data Product Group, 2021), global climatologies for most trace metals are not yet available. Thus, diagnostic models of trace-metal cycling first require an extrapolation for determining the global distribution of the element, which can be accomplished by machine-learning, e.g., using Artificial Neural Networks (ANNs) (Roshan et al., 2018; Roshan et al., 2020; Roshan and DeVries, 2021).

Here, we present a new diagnostic model of Ni fluxes in the global ocean. This model is used to further explore key questions regarding the global Ni cycle, such as whether Ni is significantly incorporated into diatom frustules, causes of the relatively deep concentration maximum observed for Ni, and whether Ni in surface ocean oligotrophic gyres is bioavailable. This work thus complements an earlier prognostic model of Ni biogeochemical cycling (John et al., 2022), by using a very different modeling approach.

2 Methods

2.1 General approach

This project was implemented in a combination of modeling environments. Machine learning predictions of Ni concentrations in the global ocean were performed in MATLAB, using tools available as part of the AWESOME OCIM modeling environment (John et al., 2020). Nutrient-restoring and boundary-condition modeling was performed in Julia using the AIBECS modeling framework (Pasquier, 2019). AIBECS output was then imported back into MATLAB/AWESOME OCIM for additional data processing and plotting. All code used in this project is available at https://github.com/MTEL-USC/nickel-diagnostic-model.

2.2 Producing a global climatology of dissolved Ni

Machine learning techniques provide a means to extrapolate sparse observations of Ni concentrations onto an entire global ocean model grid. Here we have started with Ni concentration data as reported in the GEOTRACES 2021 Intermediate Data Product (GEOTRACES Intermediate Data Product Group, 2021). Placing these data onto the OCIM v1.0 grid (averaging all points within each model grid cell) we fill in only 2% of wet grid cells with Ni concentrations (4756 out of 200160). Predictors used in the machine learning algorithms included World Ocean Atlas 2009 nitrate, phosphate, silicate, oxygen, salinity, and temperature, as well as depth, and the sine and cosine of latitude. The cosine of latitude has a maximum at the equator and decreases towards both poles (as opposed to sine of latitude which increases monotonically toward the north).

Three different methods were explored for their ability to reproduce observed Ni, and extrapolate to create global Ni climatology fields, including multiple linear regression (MLR), artificial neural networks (ANNs), and decision trees. Each of these three methods was tested by creating 100 prediction models, each trained on a random 10% of the gridded Ni concentration observations, using the MATLAB `fitlm`, `fitrnet`, and `fitrtree` functions. Each of the 100 models were then tested on the validation dataset comprised of the other 90% of the gridded observations. MLR, ANN, and decision tree models all performed with a similar level of skill on both training and validation datasets, with slopes for a comparison of predicted and observed Ni between 0.99 and 1.00 and R^2 values between 0.95 and 0.99 for the training dataset and 0.92 to 0.94 for the validation dataset (Table 1). Based on data from all 100 models run for each method, the MLR model appeared least prone to producing spurious data for the validation dataset (Fig. 3). The MLR model has a good fit to Ni observations over various ocean regions ($R^2 = 0.95$, Table 1, Figs. 3, 4), and is also the simplest model. Thus, we chose the MLR model to produce the global Ni climatology upon which the restoring model was built.

2.3 Smoothing nutrient distributions with a restoring model

With a global climatology of nutrient distribution and a circulation transport matrix, it should be possible, in theory, to directly calculate flux convergences for every model grid cell. In practice, however, combining raw data-derived climatologies and OCIM circulations produces results with significant numerical noise, and does not provide useful information even after averaging over large spatial regions. Thus, it is necessary in practice to first generate OCIM-compatible climatologies. These climatologies are smoother than the original climatologies from the World Ocean Atlas (for phosphate and silicate) or from the machine learning prediction (for Ni), but more importantly these climatologies are consistent with small-scale variability in water mixing and transport present with OCIM circulation matrices. Mathematically-focused descriptions of nutrient restoring models are presented in the work of Roshan, DeVries and coauthors (2015; 2017; 2018; 2021). Here we describe the process from a more practical perspective.

OCIM-compatible climatologies of Ni, phosphate, and silicate are created with nutrient restoring models built within the AIBECS modeling framework (Fig. 5). AIBECS (Algebraic Implicit Biogeochemical Elemental Cycling System) is built in the open-source Julia language and provides tools for biogeochemical modelers, with a particular focus on incorporating OCIM circulations and providing tools for rapidly computing steady-state model solutions (Pasquier et al., 2022). Using AIBECS, the concentration of tracer $\boldsymbol{x}$ is computed by restoring it towards the observed value in each grid cell ($\boldsymbol{x}_{\text{obs}}$) via the tracer equation:

$$\mathrm{d}\boldsymbol{x}/\mathrm{d}t = 0 = -\mathbf{T}\,\boldsymbol{x} + \frac{\boldsymbol{x}-\boldsymbol{x}_{\mathrm{obs}}}{\tau_{\mathrm{surf}}}(\boldsymbol{x} \geq \boldsymbol{x}_{\mathrm{obs}})(\boldsymbol{z} \leq z_{\mathrm{surf}}) + \frac{\boldsymbol{x}-\boldsymbol{x}_{\mathrm{obs}}}{\tau_{\mathrm{deep}}}(\boldsymbol{z} \leq z_{\mathrm{surf}}) \quad (1)$$

where $-\mathbf{T}\,\boldsymbol{x}$ is the transport flux divergence by physical circulation, z_{surf} is the depth separating the surface and deep oceans, and τ_{surf} and τ_{deep} are the restoring timescales in the surface and deep ocean, respectively. The flux-divergence term $-\mathbf{T}\,\boldsymbol{x}$ allows concentrations to mix and homogenize between nearby model grid cells, while the restoring timescales τ_{surf} and τ_{deep} restore model concentrations back to observations by pushing $\boldsymbol{x}$ towards $\boldsymbol{x}_{\mathrm{obs}}$. The constraint $(\boldsymbol{x} \geq \boldsymbol{x}_{\mathrm{obs}})$ assures that there is no biological uptake taking place in the surface ocean when the simulated tracer concentration is already lower than observations, and thus that negative concentrations are not determined for the surface ocean

2.4 Calculating the global transport divergences

Transport flux divergences for Ni, phosphate, and silicate were calculated 200 times using a random assortment of parameters in order to create the OCIM-compatible climatologies. For each run of the nutrient restoring model, one of ten OCIM 2 climatologies were chosen (DeVries and Holzer, 2019), a value between 1 to 9 months for τ_{surf}, a value between 5 to 20 years for τ_{deep}, and a value of z_{surf} of either 74 or 114 m, corresponding to either the upper 2 or 3 model layers.

For each of these sets of parameters, the climatology was created for Ni, phosphate and silicate using the nutrient-restoring model described above. This climatology ($\boldsymbol{x}$) was then multiplied by the transport matrix ($-\mathbf{T}$) in order to estimate the transport flux divergence. The 200 transport flux divergence estimates were averaged together to provide an averaged global distribution of flux divergences due to the circulation, which are used as the basis for further interpretation (Fig. 6).

3 Results and discussion

3.1 The factors which predict Ni concentrations in the oceans

Both MLR and decision-tree models provide a framework for evaluating which factors are most important for predicting Ni concentrations. It is important to note that this only reflects the importance of that factor in predicting Ni concentrations, and does not necessarily imply that the factor has a causal impact on Ni concentrations. Indeed, factors of high predictive importance may simply be impacted by another important process (such as biological uptake) in similar ways, or could even have a purely coincidental relationship.

For the MLR model, we evaluate the most important predictors based on the *t*-statistic for each variable in the linear regression equation (Table 2). We find that silicate is the most important predictor for Ni concentration with an average absolute value of *t* of 21.3 over all 100 fits tested, each based on just 10% of the observations. This reflects the overall similarity between silicate and Ni distributions in the oceans. Other important predictors include phosphate, oxygen, cosine of latitude, and depth (t = 5.8 ± 1.0, 5.2 ± 1.2, 4.9 ± 1.1, and 4.1 ± 1.0, respectively).

The relative importance of different factors in the decision tree algorithm is calculated based on the summed mean-square error due to splits on every predictor, divided by the total number of branch nodes. The three important predictors overall all 100 runs were the macronutrients silicate, nitrate, and phosphate (0.020 ± 0.017, 0.018 ± 0.019, and 0.014 ± 0.015, respectively). Interestingly, the standard deviation for these importance factors over the 100 models built with different training datasets was similar to, or even greater than, the absolute magnitude of the

importance factors. Yet, all 100 models performed quite well at predicting Ni concentrations of the entire dataset (Fig. 3, Table 1). This reflects the fact that very different decision tree models are able to produce similar Ni concentration distributions, taking different paths to a similar outcome.

3.2 Surface ocean uptake patterns

The net transport flux divergence of Si is negative in the surface oceans, reflecting supply of Si to the surface ocean by water transport, and being interpreted here as biological Si uptake. This transport flux is, as expected, most intense in the surface ocean at high latitudes (Figs. 6,7). Si uptake is highest between roughly 80°S and 60°S and decreases northward between 60°S and 40°S, with near-zero uptake across the oligotrophic gyres and equator. This reflects the rapid biological uptake of Si uptake by diatoms in cold, upwelling high-latitude waters.

Similarly, the transport flux of phosphate and Ni in the surface ocean is also most pronounced at high latitudes, but is more evenly distributed across latitudes (Figs. 6,7). The zonally averaged biological uptake of Ni and phosphate does not approach zero in subtropical latitudes as much it does for Si, and has a noticeable increase at the equator, presumably reflecting enhanced productivity due to equatorial upwelling. An overall similarity in the patterns of Ni and P uptake is seen when directly comparing their uptake rates (Fig. 7), where the relative uptake rates vary between 1 and 3 (μM/nM), but there is no clear patterns in the latitudinal distribution of this ratio. In contrast, Ni uptake compared to Si uptake has a clear latitudinal pattern, being greatly depressed at polar latitudes, and much higher at tropical and subtropical latitudes. These features support the conclusions from previous work suggesting that most biologically-cycled Ni is not present in diatom frustules (John et al., 2022). If significant amounts of Ni were present in diatom frustules, we would expect that surface uptake patterns of Ni would be more similar to those of Si, while in fact we find that surface ocean Ni uptake patterns are more similar to P.

Phosphate and Ni uptake patterns in the surface ocean also support our previous work suggesting that there is not a ~2 nM pool of non-bioavailable Ni. If that were the case, we would expect Ni/P uptake ratios to decrease dramatically as Ni concentrations approach 2 nM. Instead, we actually observe a slight increase in Ni/P uptake ratios in parts of the surface ocean where Ni concentrations are near 2 nM, though the differences in uptake rates are not significantly different for any Ni concentration range (Fig. 8).

3.3 Regeneration of Ni in the deep oceans

Net transport divergences of Ni, phosphate, and silicate are positive in the deep ocean, reflecting input of these elements from regeneration of sinking particles (Figs. 6, 9). For silicate this regeneration is interpreted as the redissolution of diatom frustules, while for phosphate this is interpreted as the remineralization of sinking organic matter. As expected because of the presence of Si within the refractory crystalline matrix of diatom frustules, Si is regenerated much more deeply in the water column than P. For example, 77 % of P regeneration occurs above 1000 m depth and 93 % occurs above 3000 m depth, while for Si these proportions are just 36 % and 68 %, respectively. The regeneration flux of Ni is intermediate between that of Si and that of P, with 58 % and 86 % of regeneration occurring above 1000 m and 3000 m, respectively.

There are a number of different possible explanations for the intermediate length scale of Ni regeneration (between Si and P). For example, it has been suggested that diatoms contain significant Ni within their frustules, which would suggest that soft-tissue phytoplankton Ni regenerates with P in the upper water column, while the Ni contained with the frustules

regenerates deeper in the water column along with Si (Twining et al., 2012). However, as discussed above, previous work shows that neither cultured nor natural ocean diatoms contain a significant amount of Ni within their silicate frustules (John et al., 2022). Also, the results of this diagnostic modeling exercise show that Ni uptake is coupled to P, not Si. The process by which Ni is regenerated deeper in the ocean than P is not clear. Because biological Ni is thought to be located mostly at the active site of metalloenzymes, it would be expected to be released from cells during the regeneration of macronutrients N and P. Thus, if biological uptake of Ni into soft tissue and remineralization of that Ni were the only process by which Ni is regenerated we would expect its regeneration profile to look very similar to that of P. Possible explanations for the deeper regenation of Ni include a high stoichiometric proportion of Ni in a class of organisms which remineralizes more deeply in the water column such as rapidly-sinking diatoms, the presence of a presently-unknown refractory phase of biological Ni, or the reversible scavenging onto sinking particles, which acts to slowly remove metals from the upper ocean and release them again in the deeper ocean, such that net regeneration of Ni occurs deeper in the ocean than P.

Our model calculations of preformed and regenerated P, Si, and Ni concentrations support the conclusions based on the regeneration rates calculated from the transport convergence (Fig. 10). While transport convergences provide the net *in situ* rates at which elements are regenerated, a comparison of preformed and regenerated nutrients illustrates the integrated impact of regeneration on elemental concentration over the entire timescale of deep-ocean mixing. Again we see a pattern whereby Ni regeneration appears to lie between P and Si. Specifically, by subtracting preformed P from total P we can isolate the portion of P in the deep oceans which is attributable to regeneration. Regenerated P has a distinct maximum in the upper ocean around 1000 m. In contrast regenerated Si increases towards the deep ocean, with highest values observed in the abyssal ocean. The depth distribution of regenerated Ni is intermediate between these two extremes.

4 Conclusions

An earlier mechanistic (prognostic) model of Ni cycling in the global oceans highlighted several important processes that control the distribution of nickel in the global oceans, including slower uptake of Ni compared to macronutrients from upwelling waters, slow Ni regeneration or reversible scavenging of Ni onto sinking particles, and the absence of a non-bioavailable form of Ni in the surface oceans (John et al., 2022). The work presented here complements our previous findings using a very different approach. Here we inferred the processes that control the spatial distribution of Ni in the oceans by diagnosing the transport divergences of Ni due to the ocean circulation only, without first making any assumptions about the biogeochemical processes that might underlie Ni distributions.

The diagnostic modeling approach taken here largely supports the earlier prognostic approach. We find strongly co-located patterns of Ni uptake and P uptake in the surface ocean, with both elements taken up much more substantially at lower latitudes compared to Si, which is depleted at higher latitudes, consistent with the assumption of our previous mechanistic model that Ni is not present in diatom frustules. We also find that Ni regeneration occurs deeper in the water column than P, though not as deep as silicate, which is consistent with the assumption of our previous mechanistic model that Ni is brought deeper into the ocean either due to slower Ni remineralization compared to P or via reversible scavenging.

Finally, we hope that this manuscript will serve as a useful guide for other researchers with an interest in the diagnostic modeling techniques used here. This follows in the footsteps of other recent projects such as the AWESOME OCIM (John et al., 2020), which aims to put OCIM

modeling tools in the hands of non-expert modelers, and AIBECS (Pasquier, 2019; Pasquier et al., 2022) which follows a similar approach but includes more sophisticated modeling tools, non-linear solvers, and is written in the open-source Julia language. As much as possible, this manuscript has been written in language which is approachable to an audience without a strong background in linear algebra and coding, as there are other manuscripts which present the same techniques in a more mathematically-focused fashion (Roshan and DeVries, 2017; Roshan et al., 2018; Roshan et al., 2020; Roshan and DeVries, 2021). With the advent of global-scale sampling projects such as GEOTRACES (Anderson, 2019) and BioGeoSCAPES, we anticipate a greater need for tools which facilitate the use of models by scientists with a background in fieldwork and sample analysis, and hope that this manuscript will aid in that effort.

Acknowledgements

This work was funded by the National Science Foundation award 2049639 and Simons Foundation award # 426570SP to SGJ, and Australian Research Council award DP210101650 to MH.

References

Alfano M. and Cavazza C. (2020) Structure, function, and biosynthesis of nickel-dependent enzymes. *Protein Sci.* **29**, 1071–1089.

Anderson R. F. (2019) GEOTRACES: Accelerating research on the marine biogeochemical cycles of trace elements and their isotopes. *Ann. Rev. Mar. Sci.* **12**.

Archer C., Vance D., Milne A. and Lohan M. C. (2020) The oceanic biogeochemistry of nickel and its isotopes: New data from the South Atlantic and the Southern Ocean biogeochemical divide. *Earth Planet. Sci. Lett.* **535**, 116118.

Biscéré T., Ferrier-Pagès C., Grover R., Gilbert A., Rottier C., Wright A., Payri C. and Houlbrèque F. (2018) Enhancement of coral calcification via the interplay of nickel and urease. *Aquat. Toxicol.* **200**, 247–256.

DeVries T. (2014) The oceanic anthropogenic CO2 sink: Storage, air-sea fluxes, and transports over the industrial era. *Global Biogeochem. Cycles* **28**, 631–647.

DeVries T. and Holzer M. (2019) Radiocarbon and Helium Isotope Constraints on Deep Ocean Ventilation and Mantle-3He Sources. *J. Geophys. Res. Ocean.* **124**, 3036–3057.

Dupont C. L., Barbeau K. and Palenik B. (2008) Ni Uptake and Limitation in Marine Synechococcus Strains. *Appl. Environ. Microbiol.* **74**, 23–31.

GEOTRACES Intermediate Data Product Group (2021) The GEOTRACES Intermediate Data Product 2021 (IDP2021). *NERC EDS Br. Oceanogr. Data Cent. NOC*, DOI: 10.5285/cf2d9ba9-d51d-3b7c-e053-8486abc0f5fd.

John S. G., Kelly R. L., Bian X., Fu F., Smith M. I., Lanning N. T., Liang H., Pasquier B., Seelen E. A., Holzer M., Wasylenki L., Conway T. M., Fitzsimmons J. N., Hutchins D. A. and Yang S.-C. (2022) The biogeochemical balance of oceanic nickel cycling. *Nat. Geosci.*

John S. G., Liang H., Weber T., DeVries T., Primeau F., Moore K., Holzer M., Mahowald N., Gardner W., Mishinov A., Richardson M. J., Faugere Y. and Taburet G. (2020) AWESOME OCIM: A simple, flexible, and powerful tool for modeling elemental cycling in the oceans. *Chem. Geol.* **533**, 119403.

John S. and Sunda W. (2018) Trace Metal Nutrients. In *Encyclopedia of Ocean Sciences, 3rd Ed.* (eds. J. K. Cochran, H. J. Bokuniewicz, and P. L. Yager). Elsevier. pp. 208–217.

Konhauser K. O., Pecoits E., Lalonde S. V, Papineau D., Nisbet E. G., Barley M. E., Arndt N. T., Zahnle K. and Kamber B. S. (2009) Oceanic nickel depletion and a methanogen famine before the Great Oxidation Event. *Nature* **458**, 750–753.

Lemaitre N., Du J., de Souza G. F., Archer C. and Vance D. (2022) The essential bioactive role of nickel in the oceans: Evidence from nickel isotopes. *Earth Planet. Sci. Lett.* **584**, 117513.

Mackey D. J., O'Sullivan J. E., Watson R. J. and Dal Pont G. (2002) Trace metals in the Western Pacific: temporal and spatial variability in the concentrations of Cd, Cu, Mn and Ni. *Deep Sea Res. Part I Oceanogr. Res. Pap.* **49**, 2241–2259.

Pasquier B. (2019) AIBECS.jl: The ideal tool for simple global marine biogeochemistry models.

Pasquier B., Primeau F. W. and John S. G. (2022) AIBECS.jl: A tool for exploring global marine biogeochemical cycles. *J. Open Source Softw.* **7**, 3814.

Price N. M. and Morel F. M. M. (1991) Colimitation of phytoplankton growth by nickel and nitrogen. *Limnol. Oceanogr.* **36**, 1071–1077.

Qiu B. and Price N. M. (2009) Different physiological responses of four marine Synechococcus strains (cyanophyceae) to nickel starvation under iron-replete and iron-deplete conditions. *J. Phycol.* **45**, 1062–1071.

Roshan S. and DeVries T. (2017) Efficient dissolved organic carbon production and export in the oligotrophic ocean. *Nat. Commun.* **8**, 2036.

Roshan S. and DeVries T. (2021) Global Contrasts Between Oceanic Cycling of Cadmium and

Phosphate. *Global Biogeochem. Cycles* **35**, e2021GB006952.
Roshan S., DeVries T. and Wu J. (2020) Constraining the Global Ocean Cu Cycle With a Data-Assimilated Diagnostic Model. *Global Biogeochem. Cycles* **34**, e2020GB006741.
Roshan S., DeVries T., Wu J. and Chen G. (2018) The Internal Cycling of Zinc in the Ocean. *Global Biogeochem. Cycles* **32**, 1833–1849.
Roshan S. and Wu J. (2015) The distribution of dissolved copper in the tropical-subtropical north Atlantic across the GEOTRACES GA03 transect. *Mar. Chem.* **176**, 189–198.
Schlitzer R., Anderson R. F., Dodas E. M., Lohan M., Geibert W., Tagliabue A., Bowie A., Jeandel C., Maldonado M. T., Landing W. M., Cockwell D., Abadie C., Abouchami W., Achterberg E. P., Agather A., Aguliar-Islas A., van Aken H. M., Andersen M., Archer C., Auro M., de Baar H. J., Baars O., Baker A. R., Bakker K., Basak C., Baskaran M., Bates N. R., Bauch D., van Beek P., Behrens M. K., Black E., Bluhm K., Bopp L., Bouman H., Bowman K., Bown J., Boyd P., Boye M., Boyle E. A., Branellec P., Bridgestock L., Brissebrat G., Browning T., Bruland K. W., Brumsack H.-J., Brzezinski M., Buck C. S., Buck K. N., Buesseler K., Bull A., Butler E., Cai P., Mor P. C., Cardinal D., Carlson C., Carrasco G., Casacuberta N., Casciotti K. L., Castrillejo M., Chamizo E., Chance R., Charette M. A., Chaves J. E., Cheng H., Chever F., Christl M., Church T. M., Closset I., Colman A., Conway T. M., Cossa D., Croot P., Cullen J. T., Cutter G. A., Daniels C., Dehairs F., Deng F., Dieu H. T., Duggan B., Dulaquais G., Dumousseaud C., Echegoyen-Sanz Y., Edwards R. L., Ellwood M., Fahrbach E., Fitzsimmons J. N., Russell Flegal A., Fleisher M. Q., van de Flierdt T., Frank M., Friedrich J., Fripiat F., Fröllje H., Galer S. J. G., Gamo T., Ganeshram R. S., Garcia-Orellana J., Garcia-Solsona E., Gault-Ringold M., George E., Gerringa L. J. A., Gilbert M., Godoy J. M., Goldstein S. L., Gonzalez S. R., Grissom K., Hammerschmidt C., Hartman A., Hassler C. S., Hathorne E. C., Hatta M., Hawco N., Hayes C. T., Heimbürger L.-E., Helgoe J., Heller M., Henderson G. M., Henderson P. B., van Heuven S., Ho P., Horner T. J., Hsieh Y.-T., Huang K.-F., Humphreys M. P., Isshiki K., Jacquot J. E., Janssen D. J., Jenkins W. J., John S., Jones E. M., Jones J. L., Kadko D. C., Kayser R., Kenna T. C., Khondoker R., Kim T., Kipp L., Klar J. K., Klunder M., Kretschmer S., Kumamoto Y., Laan P., Labatut M., Lacan F., Lam P. J., Lambelet M., Lamborg C. H., Le Moigne F. A. C., Le Roy E., Lechtenfeld O. J., Lee J.-M., Lherminier P., Little S., López-Lora M., Lu Y., Masque P., Mawji E., Mcclain C. R., Measures C., Mehic S., Barraqueta J.-L. M., van der Merwe P., Middag R., Mieruch S., Milne A., Minami T., Moffett J. W., Moncoiffe G., Moore W. S., Morris P. J., Morton P. L., Nakaguchi Y., Nakayama N., Niedermiller J., Nishioka J., Nishiuchi A., Noble A., Obata H., Ober S., Ohnemus D. C., van Ooijen J., O'Sullivan J., Owens S., Pahnke K., Paul M., Pavia F., Pena L. D., Peters B., Planchon F., Planquette H., Pradoux C., Puigcorbé V., Quay P., Queroue F., Radic A., Rauschenberg S., Rehkämper M., Rember R., Remenyi T., Resing J. A., Rickli J., Rigaud S., Rijkenberg M. J. A., Rintoul S., Robinson L. F., Roca-Martí M., Rodellas V., Roeske T., Rolison J. M., Rosenberg M., Roshan S., Rutgers van der Loeff M. M., Ryabenko E., Saito M. A., Salt L. A., Sanial V., Sarthou G., Schallenberg C., Schauer U., Scher H., Schlosser C., Schnetger B., Scott P., Sedwick P. N., Semiletov I., Shelley R., Sherrell R. M., Shiller A. M., Sigman D. M., Singh S. K., Slagter H. A., Slater E., Smethie W. M., Snaith H., Sohrin Y., Sohst B., Sonke J. E., Speich S., Steinfeldt R., Stewart G., Stichel T., Stirling C. H., Stutsman J., Swarr G. J., Swift J. H., Thomas A., Thorne K., Till C. P., Till R., Townsend A. T., Townsend E., Tuerena R., Twining B. S., Vance D., Velazquez S., Venchiarutti C., Villa-Alfageme M., Vivancos S. M., Voelker A. H. L., Wake B., Warner M. J., Watson R., van Weerlee E., Alexandra Weigand M., Weinstein Y., Weiss D., Wisotzki A., Woodward E. M. S., Wu J., Wu Y., Wuttig K., Wyatt N., Xiang Y., Xie R.

C., Xue Z., Yoshikawa H., Zhang J., Zhang P., Zhao Y., Zheng L., Zheng X.-Y., Zieringer M., Zimmer L. A., Ziveri P., Zunino P. and Zurbrick C. (2018) The GEOTRACES Intermediate Data Product 2017. *Chem. Geol.* **493**.

Tuo S., Rodriguez I. B. and Ho T.-Y. (2020) H2 accumulation and N2 fixation variation by Ni limitation in Cyanothece. *Limnol. Oceanogr.* **65**, 377–386.

Twining B. S., Baines S. B., Vogt S. and Nelson D. M. (2012) Role of diatoms in nickel biogeochemistry in the ocean. *Global Biogeochem. Cycles* **26**.

Wang S.-J., Rudnick R. L., Gaschnig R. M., Wang H. and Wasylenki L. E. (2019) Methanogenesis sustained by sulfide weathering during the Great Oxidation Event. *Nat. Geosci.* **12**, 296–300.

Wen L.-S., Jiann K.-T. and Santschi P. H. (2006) Physicochemical speciation of bioactive trace metals (Cd, Cu, Fe, Ni) in the oligotrophic South China Sea. *Mar. Chem.* **101**, 104–129.

Zhao Z., Shen B., Zhu J.-M., Lang X., Wu G., Tan D., Pei H., Huang T., Ning M. and Ma H. (2021) Active methanogenesis during the melting of Marinoan snowball Earth. *Nat. Commun.* **12**, 955.

	Training dataset		Validation dataset		Full dataset	
Model	R^2	slope	R^2	slope	R^2	slope
Multiple linear regression	0.95	0.992	0.94	0.992	0.94	0.992
Artificial Neural Network	0.97	0.996	0.95	0.995	0.95	0.996
Decision Tree	0.99	0.994	0.92	0.994	0.93	0.994

Table 1. Performance of the three different models used to predict global Ni concentrations, including multiple linear regressions, regression neural networks, and regression decision trees. The fit between observations and model predicted concentrations (R^2) and slope of observations compared to model prediction is presented as the average for 100 different models of each type, where each model was run on a training set comprised of a random 10 % of the observations, a validation dataset comprised of the other 90 % of observations, and the full dataset containing all observations.

Prediction factor	Multiple linear regression $\|t\|$	Decision tree predictor importance
Intercept	1.5 ± 1.1	-
Phosphate	5.8 ± 1.0	0.014 ± 0.015
Nitrate	0.8 ± 0.6	0.018 ± 0.019
Silicate	21.3 ± 1.8	0.020 ± 0.017
Oxygen	5.2 ± 1.2	0.0004 ± 0.0003
Temperature	1.0 ± 0.7	0.0007 ± 0.0008
Salinity	1.9 ± 1.2	0.0007 ± 0.0004
Depth	4.1 ± 1.0	0.0001 ± 0.0001
sine latitude	0.7 ± 0.5	0.0004 ± 0.0004
cosine latitude	4.9 ± 1.1	0.0001 ± 0.0001

Table 2. The importance of various predictors used in the linear regression and decision tree to predict Ni concentrations, reported as the absolute value of the *t*-statistic for linear models and the predictor importance (see text for a full description) for the decision trees. Values are reported as the average for 100 models, each trained on 10 % of the observational data, and the standard deviation for those models.

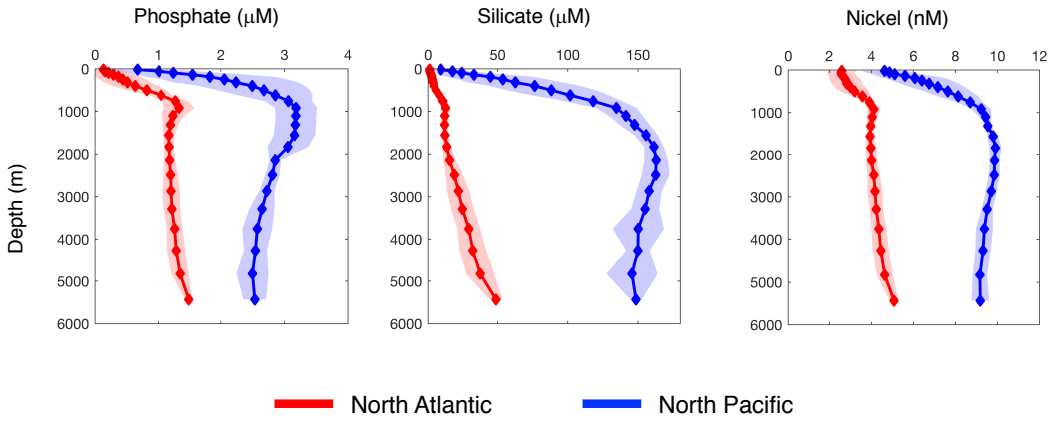

Figure 1. Phosphate, silicate, and nickel concentrations in the North Atlantic and North Pacific oceans between 35° N and 65.6° N, taken from the GEOTRACES 2017 Intermediate Data Product. Mean and std from IDP17?

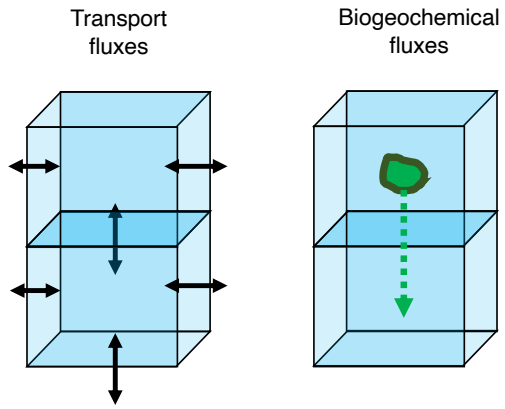

Figure 2. The diagnostic modeling approach first calculates the steady-state transport fluxes of the dissolved element into and out of every model grid cell with water mixing and advection. Any net gain or loss of the element from physical transport can subsequently be attributed to a biogeochemical process, such as loss of a nutrient element from surface boxes by incorporation into phytoplankton biomass and sinking of those particles, or a source of the element in the deeper ocean due to particle remineralization.

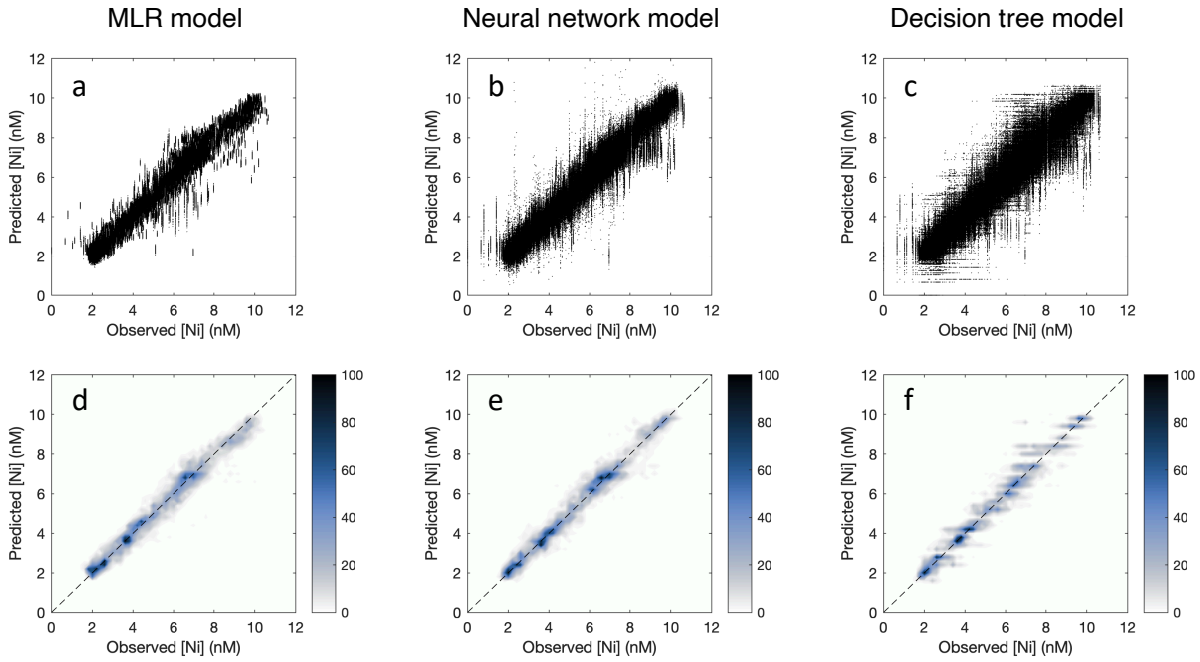

Figure 3. Three different types of models were used to predict the concentrations of Ni in the oceans. One hundred models were constructed using each approach, with each individual model based on 10 % of the Ni observations from the GEOTRACES 2021 Intermediate Data Product and then tested by comparing observed and model-predicted Ni on the full dataset. Shown here are the results of all 100 tests, both showing every pair of observations and model predictions (a-c) and as the percentile data density in a probability density function (d-f).

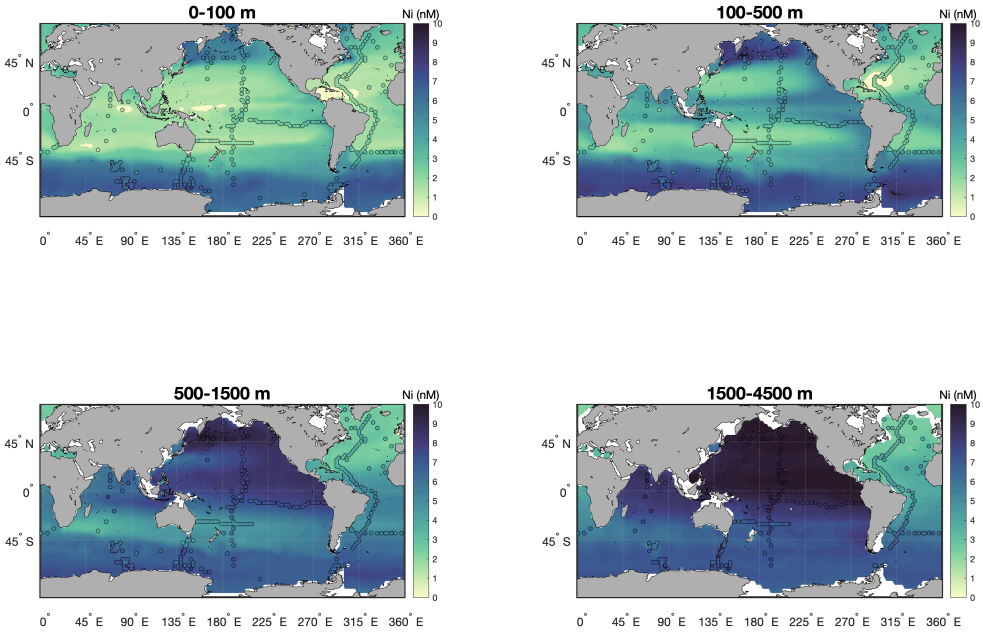

Figure 4. Nickel observations from the 2021 GEOTRACES Intermediate Data Product (circles) are compared with Ni concentrations predicted from the multiple linear regression (MLR) model, shown here averaged over different depth horizons.

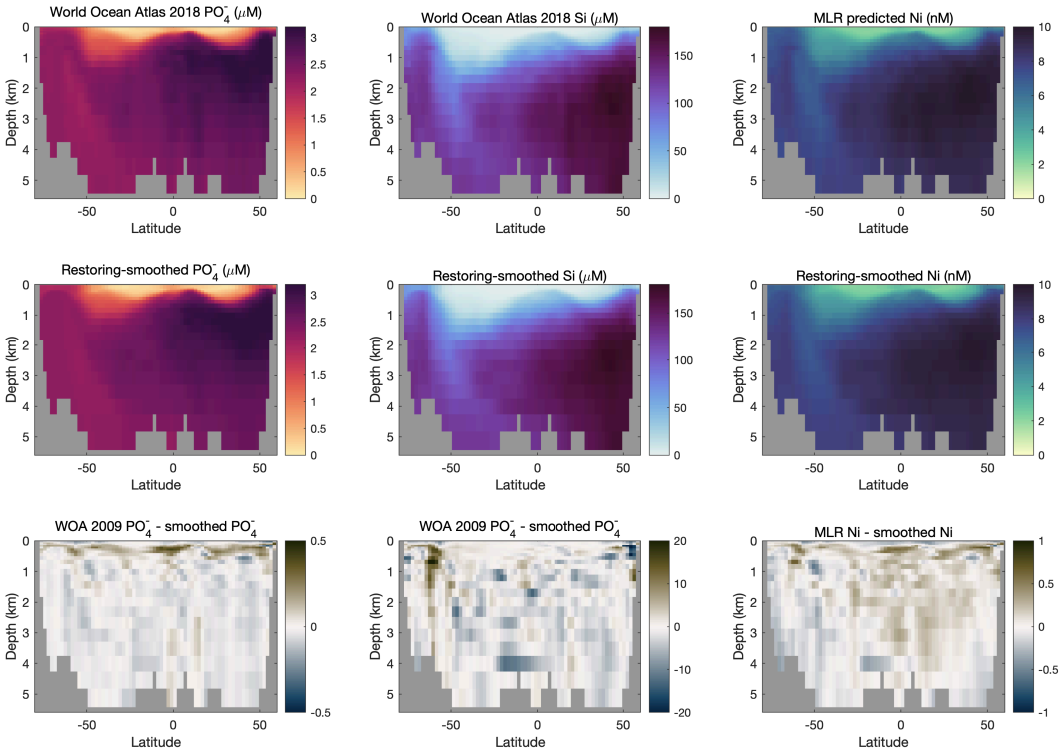

Figure 5. A comparison of the observational data before and after processing through a nutrient-restoring model. Phosphate and silicate data from the 2009 World Ocean Atlas is gridded onto the OCIM model grid, while nickel is predicted using a multiple linear regression. All data is shown as along a single representative transect through the Pacific Ocean at 161° W, and smoothing-restored distributions reflect the model output from a single run of the nutrient-restoring model.

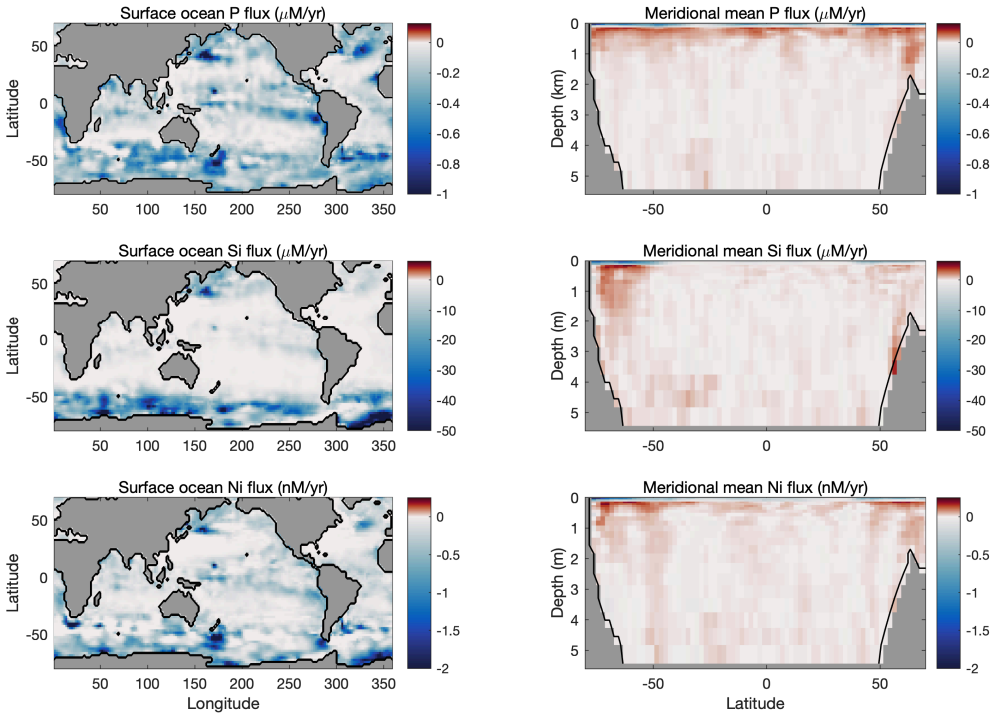

Figure 6. Global ocean fluxes of phosphate, silicate and nickel calculated as the transport divergence, such that a negative transport divergence in the surface ocean reflects net supply by transport and can be interpreted as being balanced by biological uptake, and the positive transport divergences in the deeper ocean reflect net removal by transport and are interpreted as reflecting input from regeneration.

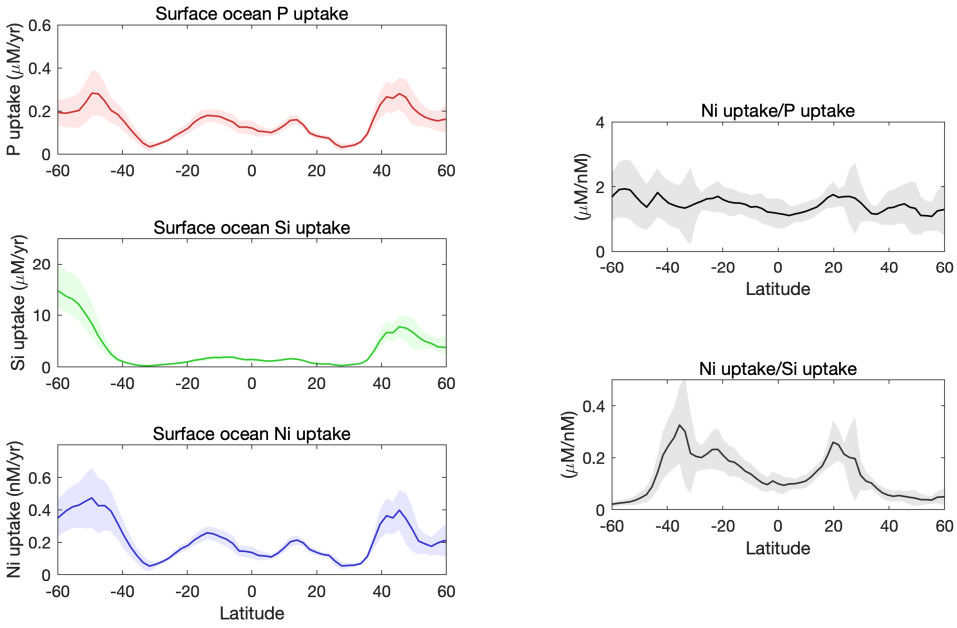

Figure 7. Global meridional mean nutrient transport convergences in the surface ocean, interpreted here as reflecting the biological uptake of phosphate, silicate, and nickel. Also shown are the relative rates of Ni/P uptake and Ni/Si uptake. Shaded regions represent the 1σ standard deviation across the 200 different nutrient restoring models used for this study.

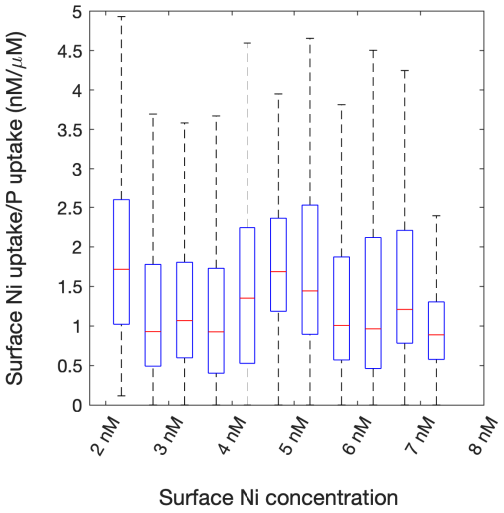

Figure 8. The ratio of surface Ni uptake to P uptake in the surface oceans are binned based on Ni concentration, in order to show that the relative Ni uptake rates do not decrease as Ni approaches 2 nM. Shown are the median value (red lines), 25th and 75th percentile (blue boxes), and total extent of the data (black dashed lines).

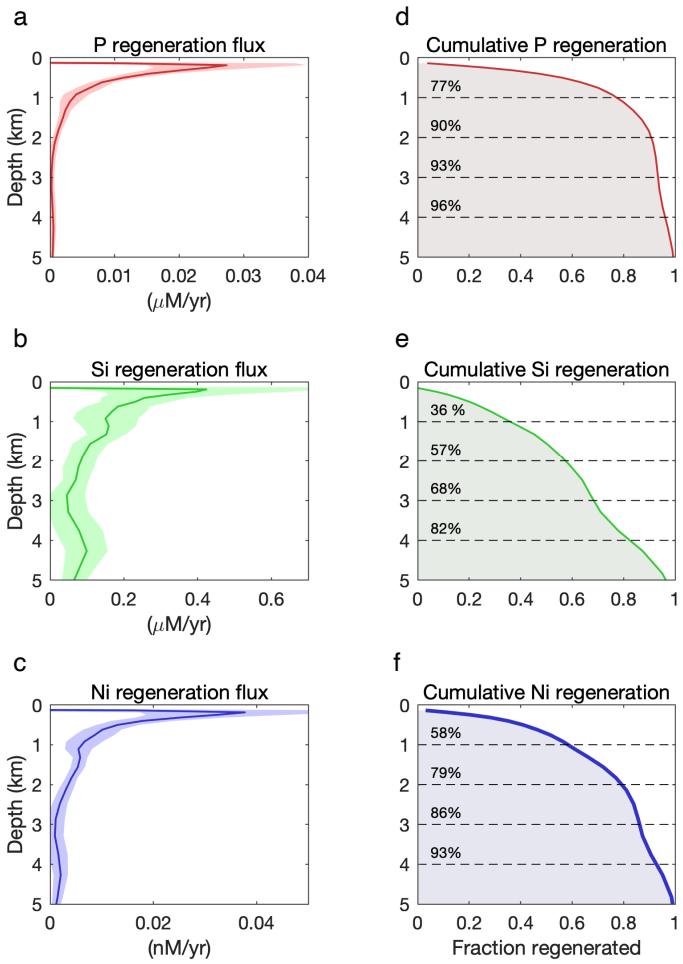

Figure 9. Global average depth profiles of the nutrient transport divergence, interpreted here as reflecting the net regeneration of phosphate, silicate, and nickel, where the shaded regions represent the 1σ standard deviation across the 200 different nutrient restoring models used for this study (a-c). Each profile is also summed and normalized to the total regeneration flux in order to show the cumulative regeneration with depth (d-f).

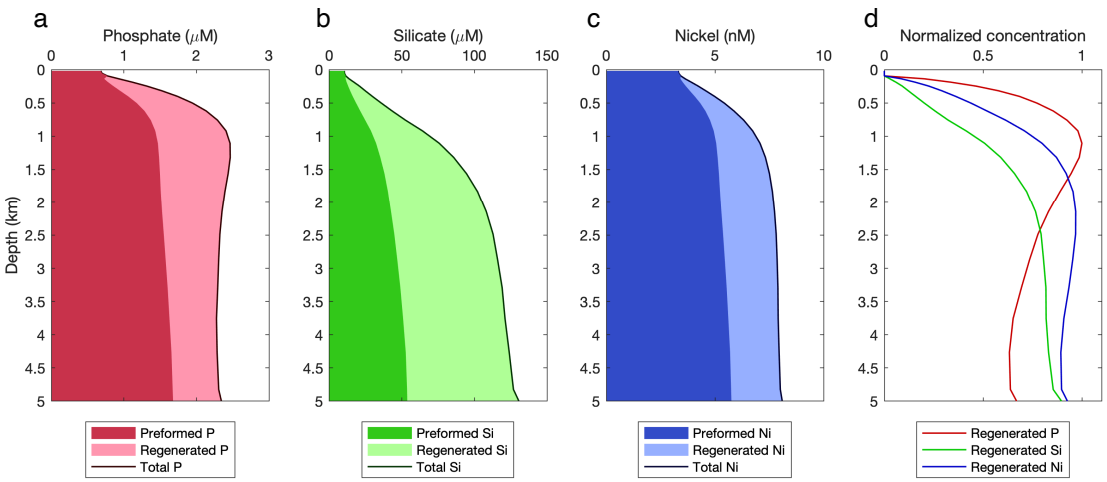

Figure 10. Globally averaged preformed and regenerated concentrations of phosphate, silicate, and nickel are shown as the darker and lighter shaded areas, respectively, while the total concentrations plotted as dark lines are simply the sum of these two (a-c). The global average concentrations of regenerated phosphate, silicate, and nickel are also plotted together in order to better compare their depth distributions, normalized to the maximum concentration (d).